Supplementary Material

1. Crystal structure of hcp and dhcp FeH_x

Fig. S1 (a) and (b) represent the primitive unit cells of stoichiometoric FeH, which is plotted by using the VESTA program (Momma and Izumi, 2011). Fig. S1 (a) contains two Fe atoms located at (0, 0, 0) and (1/3, 2/3, 1/2) position in fractional coordinate of the hexagonal lattice. Neglecting H atoms, these Fe atoms construct a hexagonal closed pack (hcp) structure. In our FeH calculation, we assumed that two H atoms initiate the octahedral interstitial sites, i.e. (2/3, 1/3, 1/4) and (2/3, 1/3, 1/4). We simply refer this crystal to hcp FeH. Similarly, Fig. S1 (b) indicates the primitive unit cell of double hexagonal close packed (dhcp) FeH. In this structure, four Fe atoms are located at (0, 0, 0), (1/3, 2/3, 1/4), (0, 0, 1/2) and (2/3, 1/3, 3/4) in the hexagonal lattice, which form a dhcp structure, and four H atoms placed at four octahedral interstitial sites, (2/3, 1/3, 1/8), (2/3, 1/3, 3/8), (1/3, 2/3, 5/8) and (1/3, 2/3, 7/8). Although previous studies (Antonov et al., 1998; Tsumuraya et al., 2012) suggested that H positions are slightly shifted along the *c* axis, this effect was ignored in our model, which may not significantly affect the calculated total energy. We also neglected the possibility that H atoms enter the other sites, such as tetrahedral interstitial site and the effect of stacking faults (Antonov et al., 1998; Ishikawa et al., 2011). Consequently, we focused on the effect of magnetism and octahedral interstitial hydrogen.

In order to simulate the effect of chemically and/or magnetic disorder, we applied the coherent potential approximation (CPA) combined with the Korringa-Kohn-Rostoker (KKR) green function method, which is implemented in AkaiKKR program package (Akai, 1989). The KKR-CPA has been widely used in solid state physics (see a recent review by Ebert et al., 2011), however, only a few groups have been used in geophysical

literatures (e.g. Koči et al., 2007; Ekholm et al., 2011; Gomi et al., 2016). Therefore, we briefly review the idea and the advantage of the CPA.

Fig. S2 (a) shows a schematic drawing of stoichiometric FeH. Gray circles represent Fe atoms. H atoms are located at the interstitial region shown by blue circles. Fig. S2 (b) shows a schematic of non-stoichiometric FeH_x with vacancy represented as blue broken lines. In the real system, non-stoichiometric FeH_x forms the chemically disordered structure. H atoms and vacancies are randomly occupied the interstitial sites without any long-range ordering. In other words, the non-stoichiometric FeH_x is an alloy or a solid solution of H atoms and vacancies. Fig. S2 (c) illustrates the idea of the supercell method, which is widely used to simulate crystals with impurity in geophysical literatures (e.g. Caracas, 2015; Umemoto and Hirose, 2015). However, the supercell method has three problems. First, the super cell method requires a large cell to simulate, especially for dilute impurity system. Second, the calculation results may depend on the atomic configuration in the supercell, so that many calculations are required with various configurations to confirm the geometry effect. The third one is that the super cell method cannot calculate the broadening of the band structure due to chemical and/or magnetic disorder (Fig. 4), because of artificial boundary condition. This broadening feature is closely related to the electrical resistivity via the uncertainty relationship between energy and life time of electrons (e.g. Gomi et al. 2016). To solve these problems, we used an alternative approach; the coherent potential approximation (CPA), which can calculate the band structure and total energy of configurational average of alloys with arbitrary concentration of impurities within a primitive cell (Fig. S2 d).

It should be noted that the total energy, volume and other extensive variables in this

study are normalized in a unit of one chemical formula, i.e. FeH_x. In case of hcp FeH_x, the primitive cell contains two Fe atoms and 2x H atoms, so that totally 2 + 2x atoms (Fig.S1 a). Similarly, dhcp FeH_x have totally 4 + 4x atoms in the primitive cell (Fig. S1 b). In order to compare the extensive variables, these quantities are normalized in a unit of FeH_x. For example, V (Bohr^3/f.u.) means the volume of polyhedron, which contains one Fe atoms and x H atoms on average, and thus, it corresponds to half of hcp calculation cell (Fig.S1 a) or quarter of dhcp calculation cell (Fig.S1 b). In case of pure Fe, it is equivalent to the atomic volume.

2. Treatment of magnetism

In this study, we computed three types of magnetic state; the ferromagnetic state, the non-magnetic state and the local magnetic disorder (LMD) state.

In spin-polarized calculations, band structure calculation programs find the metastable magnetic moment so that the total energy becomes local minimum. This implies that there are possible multiple solutions with respect to the magnetism. For example, one can find two solutions in calculation of hcp Fe at V = 75 (Bohr^3/f.u.) (Fig.1 a); one is the ferromagnetic and the other is the nonmagnetic solution. We further calculate the total energy as function of bulk magnetic moment by using the fixed spin moment procedure (Fig. S3). The results clearly show a local minimum at ~2.5 μ_B, which is a metastable solution of spin-polarized calculation. To avoid this kind of metastable phase, we conducted both of spin-polarized and non-spin-polarized calculations. In non-spin-polarized calculations, the local magnetic moments are restricted to be zero, so that only non-magnetic states can be obtained.

Fig. S4 (a) is a schematic drawing of ferromagnetic state of FeH. Arrows indicate the

local magnetic moments of each Fe sites. At the ground state, these magnetic moments align completely. However, such magnetic directions of local magnetic moments fluctuate at finite temperature. With increasing temperature, the fluctuations become large. At the Curie temperature, the alignments are completely randomized and the bulk magnetic moment becomes zero (Fig. S4 b). We refer this magnetic state as the Curie paramagnetic state. Note that, in the Curie paramagnetic state, local magnetic moments still remain, whereas the non-magnetic state (the Pauli paramagnetic state) has no local magnetic moment, which can be obtained from non-spin-polarized calculations. In order to calculate the electronic band structure at the Curie temperature within the collinear magnetism, we introduced the local magnetic disorder (LMD) state as an analog of the Curie paramagnetic state (Fig. S4 c). Note that the LMD state is a binary alloy of spin states; one component is Fe with up spin and the other is down spin. This state can be calculated by using the CPA with the alloy analogy (Ebert et al., 2015; Akai et al., 1993; Sato et al., 2003). Note also that the LMD state is not the antiferromagnetic states, which is ordered compounds of local magnetic directions. The LMD state is one of the metastable solutions, therefore, the LMD potential can be obtained from conventional self-consistent iteration procedure with an initial spin-polarized potential. The energy difference between ferromagnetic state and the LMD state corresponds to the Curie temperature via the Heisenberg model (Sato et al., 2003).

3. Finite temperature effect on H impurity resistivity

We conducted the band structure calculations only for the ground state. To directly compare with experimental results or to discuss the planetary cores, it is necessary to consider the finite temperature effects. As mentioned in the main text, local DOS of H is

located at far below the Fermi energy, which means that the effect of substitutional hydrogen to the electrical resistivity should be negligibly small. Here we will speculate the effect of electron temperature to this issue.

The Fermi-Dirac distribution expresses the excitation of electrons:

$$f(\varepsilon,T)=\frac{1}{\exp\left(\frac{\varepsilon-\mu(T)}{k_BT}\right)+1} \quad \text{(S1)},$$

where ε is the energy, $\mu(T)$ is the chemical potential, k_B is the Boltzmann constant and T is the absolute temperature. At finite temperature conditions, electrons at a certain energy range at around the chemical potential contribute to the electron conduction;

$$\frac{\partial f(\varepsilon,T)}{\partial\varepsilon}=-\frac{\exp\left(\frac{\varepsilon-\mu(T)}{k_BT}\right)}{k_BT\left\{\exp\left(\frac{\varepsilon-\mu(T)}{k_BT}\right)+1\right\}^2}, \quad \text{(S2)}$$

whereas electrons at the Fermi energy only contribute at zero Kelvin. The half width at half maximum (HWHM) of $\partial f(\varepsilon, T)/\partial\varepsilon$ is expressed as follows;

$$\Delta\varepsilon=\ln\left(3+2^{\frac{3}{2}}\right)k_BT\ . \quad \text{(S3)}$$

At T = 5000 K, the HWHM was calculated to be $\Delta\varepsilon$ = 5.58× 10^{-2} (Ry), which is independent of the detail of the band structure. On the other hand, the chemical potential is controlled by the band structure. The chemical potential can be calculated from the conservation of electrons (e.g. Boness et al., 1986). The internal energy of the electron system is represented as follows;

$$u_e(T)=\int\varepsilon D(\varepsilon)\,f(\varepsilon,T)\mathrm{d}\varepsilon \quad \text{(S4)}$$

where $D(\varepsilon)$ is the density of states as function of the energy. The number of electrons

can be calculated from the following numerical integration;

$$n_e = \int D(\varepsilon) f(\varepsilon,0) \mathrm{d}\varepsilon . \quad \text{(S5)}$$

Fig. S5 represents the DOS and $\partial f(\varepsilon, T)/\partial\varepsilon$ of hcp FeH at V = 90 (Bohr^3/f.u.). We numerically solved the conservation of electrons (Eq. S4-5) at 5000 K, and the calculated chemical potential is $\mu(T)$ = –4.63 × 10^{-3} (Ry). The tail of $\partial f(\varepsilon, T)/\partial\varepsilon$ is observed down to $\varepsilon \sim$ –0.2 Ry, whereas the H bands is located below –0.4 Ry. Therefore, we concluded that the effect of interstitial hydrogen should not be significant even at high electron temperature, e.g. 5000 K.

4. Thermal evolution calculation

Based on the thermal conductivity and the present-day CMB temperature, we computed the inner core age based on the thermodynamic modeling (Labrosse 2015; Gomi et al., 2016). Here, let us briefly review the model assumptions and calculation procedure. First, the model assumed that hydrostatic equilibrium,

$$\frac{\partial P}{\partial r} = -\rho_\mathrm{d} g , \quad \text{(S6)}$$

where ρ_d is density, g is acceleration due to gravity, r is radial position from the center and P is pressure. The one-dimensional density profile can be obtained from seismic observations (e.g. Dziewonski and Anderson, 1981), and the gravity and pressure profile should be obtained from integrations,

$$g(r) = \frac{4\pi G}{r^2}\int_0^r \rho_\mathrm{d}(u)\mathrm{d}u \quad \text{(S7)}$$

$$P(r) = P_\mathrm{ref} - \int_{r_\mathrm{ref}}^r \rho_\mathrm{d}(u) g(u) \mathrm{d}u . \quad \text{(S8)}$$

Similarly, temperature profile can be calculated based on the assumption that the outer core is isentropic,

$$T(r,t) = T_{\mathrm{CMB}}(t)\left(\frac{\rho_{\mathrm{d}}(r)}{\rho_{\mathrm{d,CMB}}}\right)^{\gamma}, \tag{S9}$$

where γ is a constant Grüneisen parameter (Vočadlo et al., 2003). Instead of numerical integration, we used 4th-order polynomial expressions given by Labrosse (2015) for density, gravity and pressure profiles, which well reproduce the PREM, and is sufficiently accurate to calculate the isentropic temperature (Labrosse, 2015).

Temporal evolution of the Earth's core can be computed by solving the following ordinary differential equations (ODE) backward with present-day CMB temperature and the inner core radius $r_{\mathrm{IC}p}$ = 1221 km as initial conditions. For the after the inner core nucleation era, the ODE is expressed based on the global energy balance as:

$$Q_{\mathrm{CMB}}(t) = \left(P_C(r_{\mathrm{IC}}) + P_L(r_{\mathrm{IC}}) + P_\chi(r_{\mathrm{IC}})\right)\frac{\mathrm{d}r_{\mathrm{IC}}}{\mathrm{d}t} + h(t)M_N \tag{S10}$$

where $Q_{\mathrm{CMB}}(t)$ is the CMB heat flow as function of time, *t*. $P_{\mathrm{c}}(r_{\mathrm{IC}})$, $P_{\mathrm{L}}(r_{\mathrm{IC}})$, $P_\chi(r_{\mathrm{IC}})$ are the secular cooling, latent heat and compositional energy terms, respectively (Labrosse 2015). The specific representation of $P_{\mathrm{X}}(r_{\mathrm{IC}})$ terms can be found written in the Appendix of Labrosse (2015). For the before onset of the inner core, the ODE is as follows:

$$Q_{CMB}(t) = P_c^* \frac{\mathrm{d}T_0}{\mathrm{d}t} + h(t)M_N \tag{S11}$$

where P_c* is a constant, which relates to the heat capacity of the core. The $h(t)M_{\mathrm{N}}$ is the contribution from radioactive elements. In this study, we assumed that no radioactive elements in the core, but it is easy to include (Gomi et al., 2016). To solve these ODEs, the time evolution of the CMB heat flow, $Q_{\mathrm{CMB}}(t)$, is required. The actual core cooling $Q_{\mathrm{CMB}}(t)$ value is regulated by surrounding thermal insulating mantle material and thus depending on the thermal conductivity and temperature gradient of thermal boundary layer developed at the mantle side of the CMB (e.g. Tateno et al., 2008; Ohta et al.,

2014). The long-time variations of these quantities are also controlled by the mantle convection regime. In this study, instead of simulating the mantle convection, we constraint the $Q_{\mathrm{CMB}}(t)$ from the heat conduction along the adiabatic temperature gradient in the core. Palaeomagnetic records suggest that the Earth's geomagnetic fields existed from at least 3.2 Ga (Tarduno et al. 2007). To maintain the geodynamo, thermal and/or chemical convective motions in the fluid metallic core are required. To generate the thermal convection, actual heat flow must be larger than the heat conduction along the adiabatic temperature gradient. Therefore, it has been believed that the geodynamo was sustained only by thermal convection before the nucleation of the inner core, and hence, the thermal conduction along the adiabat has been considered to the minimum estimate of the CMB heat flow. Recently, chemical convection mechanisms driven by MgO or SiO_2 precipitation before the onset of the inner core were proposed (O'Rourke and Stevenson, 2016; Badro et al., 2016; Hirose et al., 2017). Even though the thermal buoyancy is not the only possible convective power source, the heat conduction along the adiabatic temperature gradient may provide a good estimate for the total heat flow. Assuming that the actual CMB heat flow is always higher than the conduction along the adiabat, the previous studies computed the thermal evolution with exponential (Labrosse et al., 2001; Labrosse, 2003) or linear (Gomi et al., 2013; Labrosse, 2015) function of $Q_{\mathrm{CMB}}(t)$. In this study, we assumed that the $Q_{\mathrm{CMB}}(t)$ is always equal to the heat conduction along the adiabatic temperature gradient at the top of the core:

$$Q_{\mathrm{CMB}}(t) \approx Q_S(t) \equiv -4\pi r_{\mathrm{CMB}}^2 k_{\mathrm{CMB}}(t) \left(\frac{\partial T_{\mathrm{CMB}}(t)}{\partial r} \right)_{\mathrm{S}} \tag{S12}$$

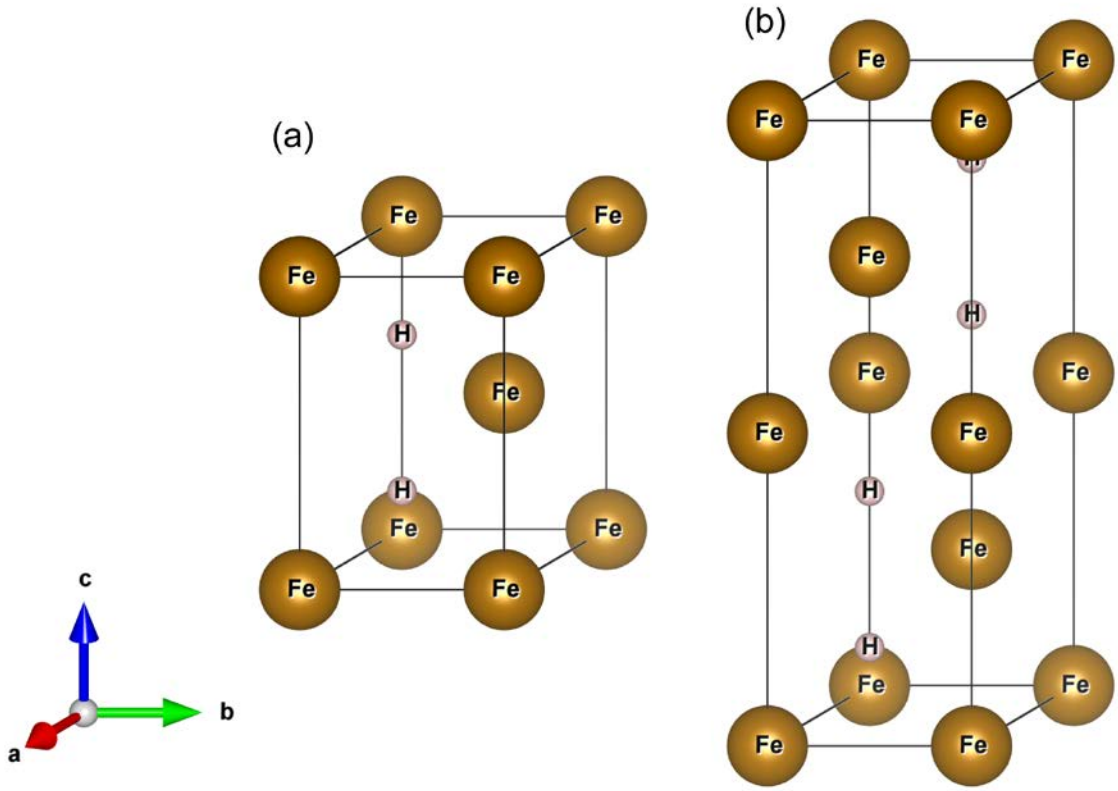

Supplementary Fig. S1. Crystal structure of hcp (a) and dhcp (b) FeH.

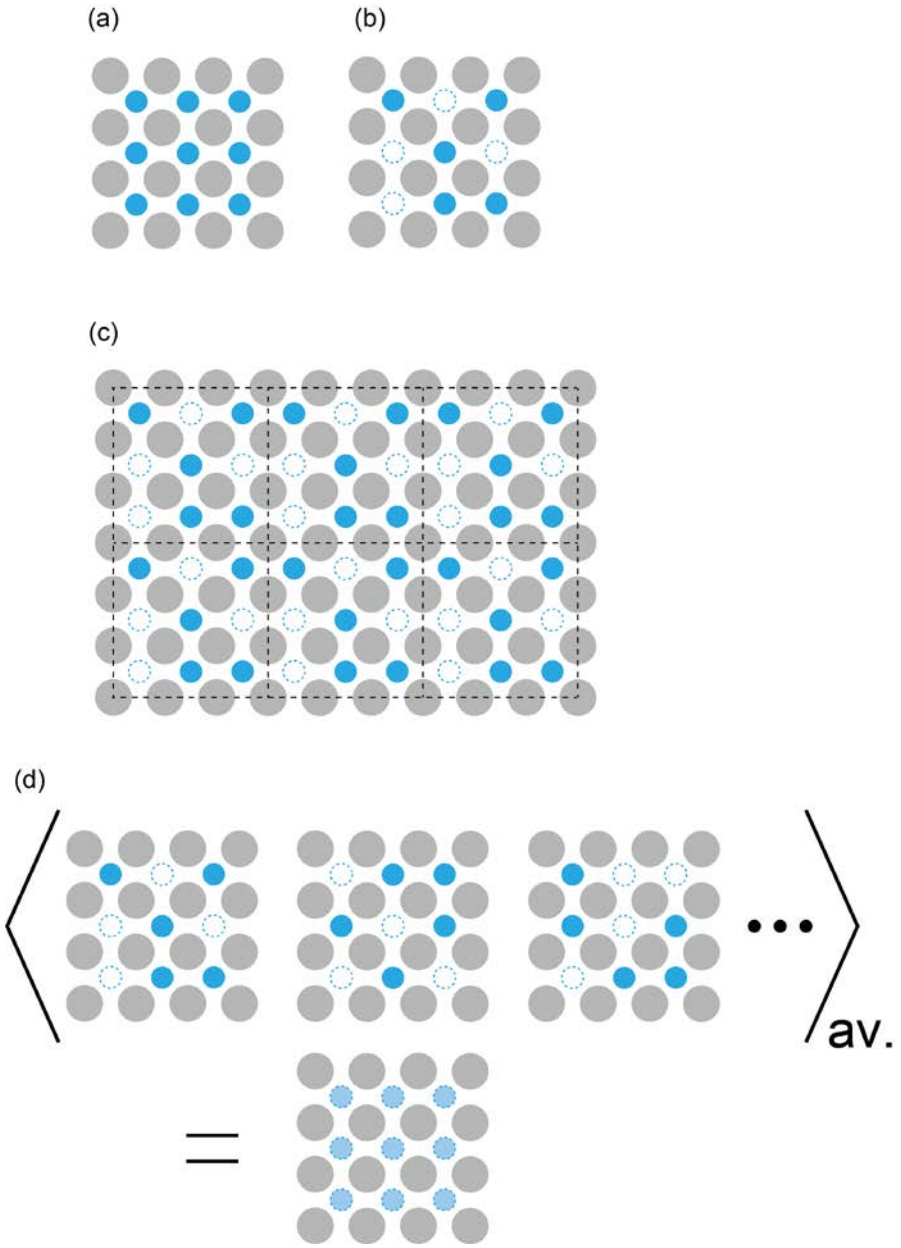

Supplementary Fig. S2. Schematic diagrams of FeH_x alloys. Gray large circles and blue small circles represent Fe and H atoms, respectively. (a) FeH; H atoms occupied all interstitial sites. (b) FeH_x; H atoms randomly occupied $100x$ % of interstitial sites. (c) The supercell method for FeH_x. (d) The coherent potential approximation (CPA) for FeH_x.

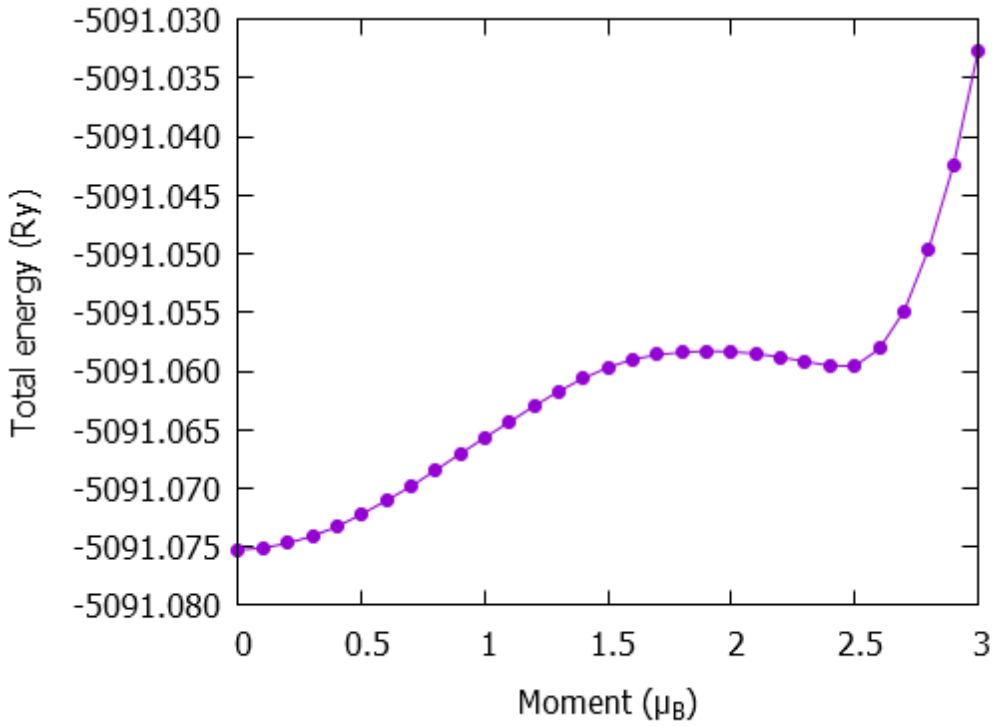

Supplementary Fig. S3. Total energy of hcp Fe at V = 75 (Bohr^3/f.u.) as function of the magnetic moment. In this plot, there are two solutions; the most stable solution is non-magnetic state, and the metastable ferromagnetic solution is also found at around 2.5 μ_B.

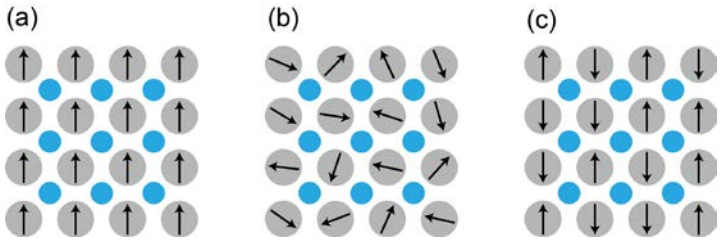

Supplementary Fig. S4. Schematic diagrams of magnetism. (a) Ferromagnetic state. (b) Paramagnetic state at the Curie temperature. (c) Local magnetic disorder (LMD) state.

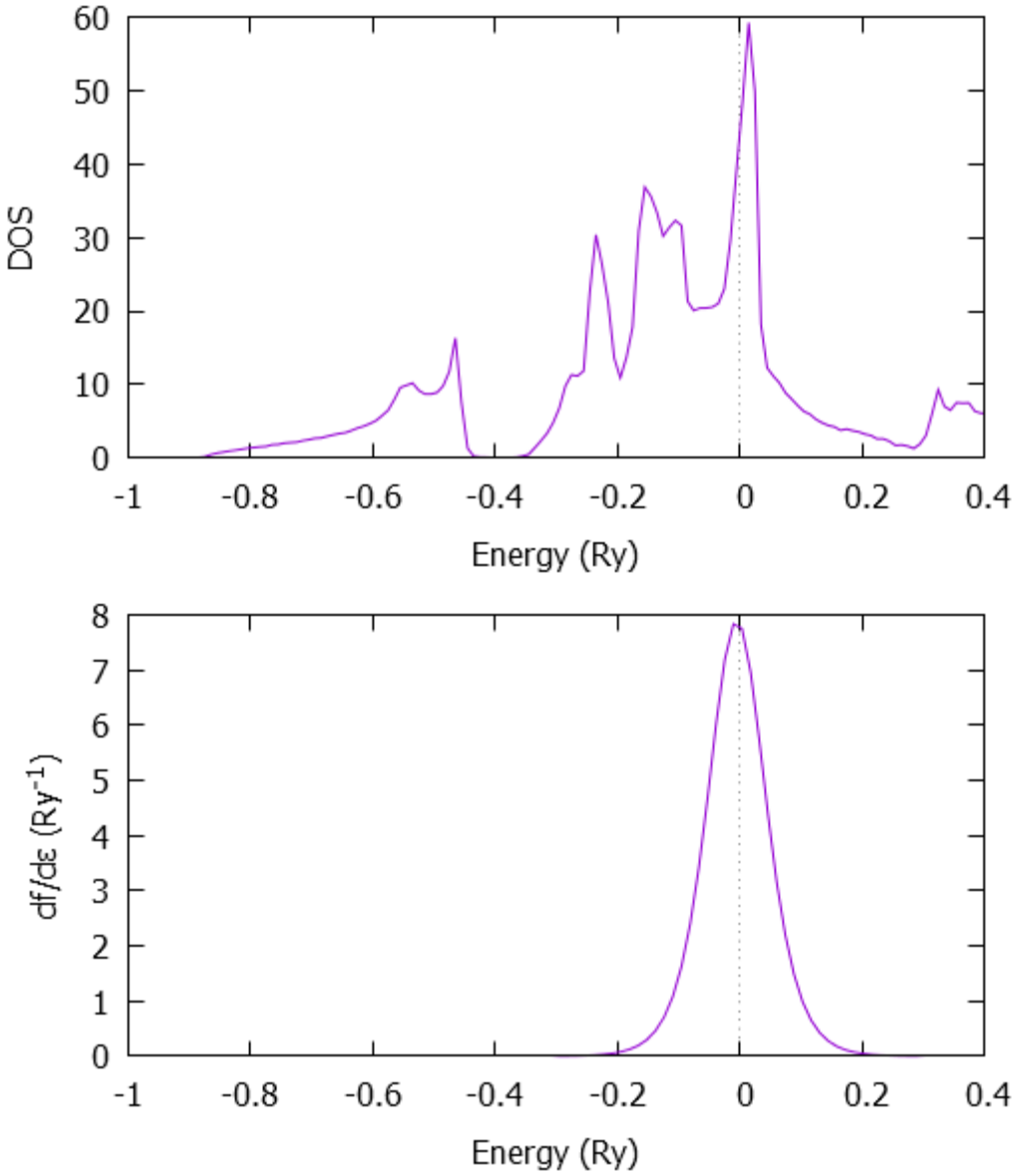

Supplementary Fig. S5. Density of states of hcp FeH at V = 90 (Bohr^3/f.u.) and energy differential of the Fermi-Dirac distribution.

References cited

Akai, H., (1989). Fast Korringa-Kohn-Rostoker coherent potential approximation and its application to FCC Ni-Fe systems, Journal of Phyics: Condenced Matter, 1(43), 8045-8063.

Akai, H., and Dederichs, P. H., (1993). Local moment disorder in ferromagnetic alloys, Physical Review B, 47(14), 8739-8747.

Antonov, V. E., Cornell, K., Fedotov, V. K., Kolesnikov, A. I., Ponyatovsky, E. G., Shiryaev, V. I., and Wipf, H. (1998). Neutron diffraction investigation of the dhcp and hcp iron hydrides and deuterides. Journal of Alloys Compounds., 264(1), 214-222.

Badro, J., Siebert, J., and Nimmo, F. (2016). An early geodynamo driven by exsolution of mantle components from Earth's core. Nature, 536(7616), 326-328.

Boness, D. A., Brown, J. M., and McMahan, A. K. (1986). The electronic thermodynamics of iron under Earth core conditions. Physics of the Earth and Planetary Intererior, 42(4), 227-240.

Caracas, R., (2015). The influence of hydrogen on the seismic properties of solid iron, Geophysical Research Letters, 42(10), 3780-3785.

Dziewonski, A. M., and Anderson, D. L. (1981). Preliminary reference Earth model. Physics of the Earth and Planetary Interior, 25(4), 297-356.

Ebert, H., Koedderitzsch, D., and Minar, J. (2011). Calculating condensed matter properties using the KKR-Green's function method-recent developments and applications. Reports on Progress in Physics, 74(9), 096501.

Ebert, H., Mankovsky, S., Chadova, K., Polesya, S., Minár, J., and Ködderitzsch, D., (2015). Calculating linear-response functions for finite temperatures on the basis of

the alloy analogy model, Physical Review B, 91(16), 165132.

Ekholm, M., Mikhaylushkin, A. S., Simak, S. I., Johansson, B., and Abrikosov, I. A. (2011). Configurational thermodynamics of Fe–Ni alloys at Earth's core conditions. Earth and Planetary Science Letters, 308(1), 90-96.

Faber, T. E., (1972). Introduction to the Theory of Liquid Metals. Cambridge at the University Press.

Gomi, H., Hirose, K., Akai, H., and Fei, Y. (2016). Electrical resistivity of substitutionally disordered hcp Fe–Si and Fe–Ni alloys: Chemically-induced resistivity saturation in the Earth's core. Earth and Planetary Science Letters, 451, 51-61.

Hirose, K., Morard, G., Sinmyo, R., Umemoto, K., Hernlund, J., Helffrich, G., and Labrosse, S. (2017). Crystallization of silicon dioxide and compositional evolution of the Earth's core. Nature, 543, 99-102.

Ishikawa, T., Tsuchiya, T., and Tsuchiya, J. (2011). Stacking-disordered phase of iron in the Earth’s inner core from first principles. Physical Review B, 83(21), 212101.

Koči, L., Vitos, L., and Ahuja, R. (2007). Ab initio calculations of the elastic properties of ferropericlase $Mg_{1-x}Fe_xO$ ($x \leq 0.25$). Physics of the Earth and Planetary Interior, 164(3), 177-185.

Labrosse, S. (2003). Thermal and magnetic evolution of the Earth’s core. Physics of the Earth and Planetary Interiors, 140(1-3), 127-143.

Labrosse, S. (2015). Thermal evolution of the core with a high thermal conductivity. Physics of the Earth and Planetary Interior, 247, 36-55.

Labrosse, S., Poirier, J. P., and Le Mouël, J. L. (2001). The age of the inner core. Earth and Planetary Science Letters, 190(3-4), 111-123.

Momma, K., and Izumi, F. (2011). VESTA 3 for three-dimensional visualization of crystal, volumetric and morphology data. Journal of Applied Crystallography 44(6), 1272-1276.

O'rourke, J. G., and Stevenson, D. J. (2016). Powering Earth's dynamo with magnesium precipitation from the core. Nature, 529(7586), 387.

Ohta, K., Yagi, T., Taketoshi, N., Hirose, K., Komabayashi, T., Baba, T., Ohishi, Y., and Hernlund, J. (2012). Lattice thermal conductivity of $MgSiO_3$ perovskite and post-perovskite at the core–mantle boundary. Earth and Planetary Science Letters, 349, 109-115.

Sato, K., Dederics, P., and Katayama-Yoshida, H., (2003). Curie temperatures of III–V diluted magnetic semiconductors calculated from first principles, Europhysics Letters, 61(3), 403-408.

Tarduno, J. A., Cottrell, R. D., Watkeys, M. K., and Bauch, D. (2007). Geomagnetic field strength 3.2 billion years ago recorded by single silicate crystals. Nature, 446(7136), 657-660.

Tateno, S., Hirose, K., Sata, N., and Ohishi, Y. (2009). Determination of post-perovskite phase transition boundary up to 4400 K and implications for thermal structure in D" layer. Earth and Planetary Science Letters, 277(1), 130-136.

Tsumuraya, T., Matsuura, Y., Shishidou, T., and Oguchi, T. (2012). First-principles study on the structural and magnetic properties of iron hydride. Journal of Physical Society of Japan, 81(6), 064707.

Umemoto, K., and Hirose, K. (2015). Liquid iron-hydrogen alloys at outer core conditions by first-principles calculations, Geophysical Research Letters, 42(18), 7513-7520.

Vočadlo, L., Alfe, D., Gillan, M. J., and Price, G. D. (2003). The properties of iron under core conditions from first principles calculations. Physics of the Earth and Planetary Interior, 140(1), 101-125.